PERGAMON

International Journal of Heat and Mass Transfer 42 (1999) 497–510

International Journal of HEAT and MASS TRANSFER

Development of secondary flow and convective heat transfer in isothermal/iso-flux rectangular ducts rotating about a parallel axis

C.Y. Soong[a,*], W.M. Yan[b]

[a] *Department of Aeronautical Engineering, Chung Cheng Institute of Technology, Tahsi, Taoyuan, Taiwan 33509, Republic of China*

[b] *Department of Mechanical Engineering, Huafan University, Taipei, Taiwan 22305, Republic of China*

Received 31 October 1997; in final form 6 May 1998

Abstract

The present study investigates rotation-induced secondary flow and mixed convection heat transfer in the entrance region of rectangular ducts rotating about a parallel axis. Boussinesq approximation is invoked to take into account the centrifugal buoyancy. Mechanisms of the secondary vortex development in ducts of isothermal or iso-flux walls are explored by a vorticity transport analysis. Numerical solutions of the parabolized velocity–vorticity formulation of Navier–Stokes/Boussinesq systems are used to corroborate the above theoretical analysis and provide evidence for the relevance of axial variation of transport rates to the evolution of the secondary vortices. The present results also reveal that the rotational effect in an iso-flux duct is more significant than that in an isothermal flux. In a fully developed flow region, the iso-flux case can still retain a secondary vortex effect, while the effect vanishes in isothermal ducts.

Nomenclature

a, b width and height of a rectangular duct, respectively [m]
D_e equivalent hydraulic diameter, $2ab/(a+b) = 2a/(1+\gamma)$
E dimensionless eccentricity of the rotating ducts, H/D_e
$\mathbf{e}_x, \mathbf{e}_y, \mathbf{e}_z$ unit vectors in (x, y, z) coordinates
f peripherally averaged friction factor, $2\tau_w/(\rho u_o^2)$
Gr_Ω rotational Grashof number, $(\Omega^2 H)\beta\Delta T_c D_e^3/\nu^2$
H radial distance from axis of rotation to centerline of duct
h peripherally averaged heat transfer coefficient [W m^{-2} K^{-1}]
J rotational Reynolds number, $\Omega D_e^2/\nu$
k thermal conductivity [W m^{-1} K^{-1}]
M, N numbers of grid points in Y and Z directions
m iteration number
n dimensionless directional normal to the duct wall
Nu peripherally averaged Nusselt number, hD_e/k
p' perturbation term about the mean pressure, $p' = p_d - p_m$
P_m, p_m dimensionless and dimensional cross-sectional mean pressure, $P_m = p_m/(\rho u_o^2)$
p_d dimensionless pressure departure from the reference state, $p_d = p - p_o = p_m + p'$ [kPa]
Pr Prandtl number, ν/α
q_w wall heat flux [W m^{-2}]
$\mathbf{R}$ radial position vector, $R_y\mathbf{e}_y + R_z\mathbf{e}_z$
R_y, R_z y- and z-components of the radial position vector
Re Reynolds number, $u_o D_e/\nu$
Ro rotation number, $\Omega D_e/u_o$
T temperature [K]
ΔT_c characteristic temperature difference, $T_w - T_o$ for UWT and $q_w D_e/k$ for UHF [K]
UHF uniform heat flux
UWT uniform wall temperature
$\mathbf{V}$ dimensionless velocity vector (U, V, W)

* Corresponding author. Tel.: 00 886 3 390 8102; Fax: 00 886 3 389 1519; E-mail: cysoong@ccit.edu.tw

0017–9310/98 $19.00
PII: S0017–9310(98)00199–9

$\mathbf{v}$ dimensional velocity vector (u, v, w) [m s^{-1}]
X^* dimensionless axial coordinate, $X^* = x(D_e/PrRe) = X/Pr$
X, Y, Z dimensionless rectangular coordinates
$X = x/(D_eRe)$, $Y = y/D_e$, $Z = z/D_e$
x, y, z Cartesian coordinates [m].

Greek symbols
α thermal diffusivity [m^2 s^{-1}]
β coefficient of thermal expansion [K^{-1}]
γ aspect ratio of the rectangular duct, a/b
θ dimensionless temperature, $(T-T_o)/\Delta T_c$
μ dynamic viscosity [Ns m^{-2}]
ν kinematic viscosity [m^2 s^{-1}]
$\boldsymbol{\xi}$ dimensionless vorticity vector, $\boldsymbol{\xi} = \mathbf{V} \times \mathbf{V}$
ρ density [kg m^{-3}]
τ_w peripherally averaged wall shear stress [kPa]
Ω, Ω^* dimensional and normalized angular velocity vector, $\Omega^* = \Omega/\Omega$
Ω angular speed of rotation [rpm].

Superscript
$\overline{(\ )}$ peripherally-averaged quantity.

Subscripts
b bulk flow quantity
j number for identification of the duct walls
o inlet or reference condition
w wall condition.

1. Introduction

Internal cooling is usually required in rotating machinery especially that operating in a high-temperature environment. Some of the cooling designs involve flow channels parallel to the rotating axis. In this situation, the coolant flow can be influenced by rotational effects including centrifugal buoyancy in non-isothermal flow. The rotation-induced secondary flow may distort the longitudinal velocity profiles as well as the temperature distributions and in turn change the heat transfer performance. The evolution of longitudinal vortex in radially rotating ducts has been studied [1, 2]; however, no buoyancy effect was involved in their discussion. The rotation-induced buoyancy effects in radial-flow passages have been investigated previously, e.g. [3, 4] for radially rotating ducts; and [5, 6] for rotating disks, to name a few.

For rotating parallel ducts, the perturbation analysis by Morris [7] was the first theoretical study of fully-developed convective heat transfer. Later, by using a boundary-layer model and accompanying experiments, Mori and Nakayama [8] and Nakayama [9] performed elegant analyses on laminar and turbulent forced convection in fast-rotating circular pipes. In their theoretical analyses, however, centrifugal buoyancy was not considered.

In experimental work on laminar [10, 11] and turbulent [12–14] entrance flow in rotating ducts of parallel mode, it was demonstrated that the rotational effect is relatively stronger in laminar flows. The increases in flow resistance due to rotation in the entrance region were typically about 30–40% in laminar flow, but under 10% in the turbulent regime. From the experiments on fully developed laminar and turbulent flows in a rotating elliptical duct [15], the increase in heat transfer lies between those for circular and square ducts.

As for the numerical investigations,the fully-developed flows in circular pipe [16], rectangular and elliptical ducts [17] have been explored. A study of rotational effect on isothermal flows developing in a parallel tube was performed by Johnson [18]. Laminar developing flow in axially rotating pipe was also studied [19, 20]. The numerical computations performed by Neti et al. [21] investigated the rotation-induced buoyancy effect in a rectangular duct of aspect ratio $\gamma = 0.5$ rotating in parallel mode. In their study, however, the centrifugal buoyancy effects on the flow and heat transfer characteristics were not addressed in detail. The experiments of developing heat transfer in an axially rotating rectangular ducts with consideration of centrifugal buoyancy were conducted by Levy et al. [22]. For high rotating rates, the test models in laboratory work are usually small in size, for which the difficulty in local flow measurement is inevitable. On the other hand, numerical simulation can inexpensively provide examination of different experimental conditions and accompanying detailed flows. Therefore, numerical computation is useful in understanding the details of the local flow characteristics.

The rectangular duct is a widely-used configuration in practical applications. Detailed flow structure and heat transfer mechanisms under the influences of rotational forces as well as various thermal boundary conditions are of academic interest, while the friction factors and heat transfer rates are of importance in practical applications. These reasons motivate the present study which treats the flow and thermal characteristics in rotating parallel rectangular ducts with consideration of the rotation-induced buoyancy effects. The first part of the paper deals with derivation of velocity–vorticity formulation of the problem and, based on the vorticity transport equation, studies the streamwise evolution of the rotation-induced secondary vortex. Then the numerical computations are performed and the numerical results can be corroborated by the conclusions of the vorticity transport analysis. The mainly concerned issues are (1) the rotational effects on flow and heat transfer; (2) the secondary flow phenomena and its relevance to the streamwise development of heat transfer and wall friction; and (3) the influences of thermal boundary condition on the development of secondary flow.

2. Theoretical analysis

2.1. Problem statement and velocity–vorticity formulation

Figure 1 shows a rectangular duct of width b and height a rotating at a constant rate Ω around an axis parallel to the duct itself. The distance between the duct center line and the rotational axis is the eccentricity H. Cartesian coordinates $Oxyz$ are attached and rotate with the duct. The coolant flow at the duct inlet lies at a uniform velocity u_o and temperature T_o. Thermal boundary conditions of the duct wall can be isothermal (uniform wall temperature, UWT), T_w, or iso-flux (uniform heat flux, UHF), q_w. In the present work, the following assumptions are employed:

(1) The flow is laminar, steady and of constant properties.
(2) Gravitational effect is neglected as compared to the centrifugal force. For example, in a case of $\Omega = 10^3$ rpm and $H = 10^{-1}$ m, one has a small ratio of gravity-to-centrifugal accelerations, $g/H\Omega^2 < 10^{-2}$.
(3) Boussinesq approximation is invoked to account for centrifugal buoyancy effect, for which a linear density–temperature relation, $\rho = \rho_o[1-\beta(T-T_o)]$ with ρ_o as the density evaluated at the reference condition, is used.
(4) Axial diffusion in momentum and energy balance are neglected for the small influences from downstream flow in the case without axial circulation. This is usually valid for the order of the Peclet number being large enough, e.g. $O(Pe) \geqslant 10^2$ [23].
(5) Compression work and viscous dissipation in energy equation are negligibly small. It is a good approximation for low Mach number flows.

By using the inlet condition as a reference state and defining a pressure departure from the reference, $p_d \equiv p - p_o$ denotes the flow pressure at the inlet, one has

$$-\partial p/\partial y + \rho\Omega^2(H-b/2+y) = -\partial p_d/\partial y - \rho\beta(T-T_o)\Omega^2(H-b/2+y) \quad (1a)$$

$$-\partial p/\partial z + \rho\Omega^2(z-a/2) = -\partial p_d/\partial z - \rho\beta(T-T_o)\Omega^2(z-a/2). \quad (1b)$$

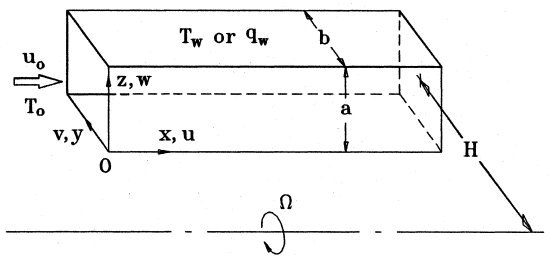

Fig. 1. Schematic diagram of the physical system.

The pressure function $p_d(x,y,z)$ is further split into a cross-sectional average, $p_m(x)$, driving the main flow and a perturbation, $p'(y,z)$, driving the cross-stream flow, i.e. $p_d(x,y,z) = p_m(x) + p'(y,z)$. Splitting pressure and ignoring axial diffusion (for Re and Pe high enough) permits a marching integration procedure [23, 24]. By considering the above assumptions and introducing the following dimensionless variables and groups

$$X = x/(D_e R_e), \quad Y = y/D_e, \quad Z = z/D_e,$$
$$U = u/u_o, \quad V = vD_e/\nu, \quad W = wD_e/\nu,$$
$$P_m = p_m/(\rho u_o^2), \quad \xi = \partial W/\partial Y - \partial V/\partial Z,$$
$$\theta = (T-T_o)/\Delta T_c, \quad Re = u_o D_e/\nu,$$
$$Pr = \nu/\alpha, \quad J = \Omega D_e^2/\nu,$$
$$Gr_\Omega = \Omega^2 H\beta\Delta T_c D_e^3/\nu^2, \quad \gamma = a/b, \quad E = H/D_e,$$

a velocity–vorticity formulation including axial momentum (U), transverse velocities (V and W), axial vorticity (ξ) and thermal energy (θ) can be developed:

$$U\partial U/\partial X + V\partial U/\partial Y + W\partial U/\partial Z = -\mathrm{d}P_m/\mathrm{d}X + \partial^2 U/\partial Y^2 + \partial^2 U/\partial Z^2 \quad (2)$$

$$\partial^2 V/\partial Y^2 + \partial^2 V/\partial Z^2 = -\partial\xi/\partial Z - \partial^2 U/\partial X\partial Y \quad (3)$$

$$\partial^2 W/\partial Y^2 + \partial^2 W/\partial Z^2 = \partial\xi/\partial Y - \partial^2 U/\partial X\partial Z \quad (4)$$

$$U\partial\xi/\partial X + V\partial\xi/\partial Y + W\partial\xi/\partial Z + \xi\partial U/\partial X + (\partial U/\partial Y\cdot\partial W/\partial X - \partial U/\partial Z\cdot\partial V/\partial X) = \partial^2\xi/\partial Y^2 + \partial^2\xi/\partial Z^2 + 2J\partial U/\partial X + Gr_\Omega[Y/E + 1 - (1+\gamma)/(4\gamma E)]\cdot\partial\theta/\partial Z - Gr_\Omega[Z/E - (1+\gamma)/(4E)]\cdot\partial\theta/\partial Y \quad (5)$$

$$U\partial\theta/\partial X + V\partial\theta/\partial Y + W\partial\theta/\partial Z = (\partial^2\theta/\partial Y^2 + \partial^2\theta/\partial Z^2)/Pr. \quad (6)$$

In the dimensionless parameters, $D_e = 2ab/(a+b)$ stands for the hydraulic diameter of the duct, and ΔT_c denotes the characteristic temperature difference and it is $T_w - T_o$ for isothermal (UWT) or $q_w D_e/k$ for iso-flux (UHF) ducts. For proper calculation of the axial pressure gradient, $-\mathrm{d}P_m/\mathrm{d}X$, the global mass conservation,

$$\int_0^{(1+\gamma)/(2\gamma)}\int_0^{(1+\gamma)/2} U\,\mathrm{d}Y\,\mathrm{d}Z = (1+\gamma)^2/(4\gamma), \quad (7)$$

has to be satisfied at each axial location. The boundary conditions are:

at walls:

$$U = V = W = 0; \quad \theta = 1 (UWT) \quad \text{or} \quad \partial\theta/\partial n = 1 \text{ (UHF)}$$

at entrance:

$$U = 1, \quad V = W = \xi = \theta = 0, \quad (8)$$

where n denotes the outward normal direction of the wall. Following the usual definitions, the peripheral averages of friction parameter, fRe, and Nusselt number,

Nu, can be expressed based on the axial velocity and temperature gradients on the duct walls, viz.

$$fRe = -2(\overline{\partial U/\partial n})_w \tag{9a}$$

$$Nu = (\overline{\partial \theta_w/\partial n})/(1-\theta_b) \tag{9b}$$

where the overbar denotes peripherally-averaged quantities. The bulk temperature θ_b is defined as

$$\theta_b = \int_0^{(1+\gamma)/(2\gamma)} \int_0^{(1+\gamma)/2} \theta U \, dY \, dZ/[(1+\gamma)^2/(4\gamma)]. \tag{10}$$

2.2. Governing parameters

By using the above non-dimensionalization, just like that mentioned in [23], the only term involving Reynolds number is dropped in parabolized procedure, and *Re* is implicitly hidden in the axial variables. The solutions depend on two geometry parameters, E and γ, and three flow/thermal parameters, J, Gr_Ω and Pr. To reduce the computational efforts, the dimensionless eccentricity of the rotating ducts is fixed to be $E = 10$, and the Prandtl number $Pr = 0.7$ for air is used in the computations. Effects of the rest three parameters are examined in detail. The rotational Reynolds number J characterizes the Coriolis effect or a measure of the relative strength of Coriolis to viscous forces. The rotational Grashof number Gr_Ω measures the significance of the centrifugal buoyancy effect. The cross-sectional aspect ratio γ is the major geometry parameter considered in the work. The flow characteristics, especially the evolution of the secondary vortices, may be significantly influenced by the change in aspect ratio. In the present study, the rotational Reynolds number J ranges from 0 to 800, the rotational Grashof number Gr_Ω lies from 0 to 1×10^6, and the ducts of $\gamma = 0.2$, 0.5, 1, 2, and 5 are considered.

2.3. Vorticity transport in rotating ducts of parallel mode

In the present nomenclature with a vorticity vector $\boldsymbol{\xi} \equiv \mathbf{V}\times\mathbf{V}$ and normalized rotation vector $\boldsymbol{\Omega}^* \equiv \boldsymbol{\Omega}/|\boldsymbol{\Omega}|$, the dimensionless vorticity transport equation is

$$(\mathbf{V}\cdot\nabla)\boldsymbol{\xi} = (\boldsymbol{\xi}\cdot\nabla)\mathbf{V} + \nabla^2\boldsymbol{\xi} + 2J\nabla\times(\boldsymbol{\Omega}^*\times\mathbf{V}) + Gr_\Omega\nabla\times[\boldsymbol{\Omega}^*\times(\boldsymbol{\Omega}^*\times\mathbf{R})\theta]$$

or

$$(\mathbf{V}\cdot\nabla)\boldsymbol{\xi} = (\boldsymbol{\xi}\cdot\nabla)\mathbf{V} + \nabla^2\boldsymbol{\xi} + 2J(\mathbf{e}_x\cdot\nabla)\mathbf{V} - Gr_\Omega\nabla\times(\mathbf{R}\theta) \tag{11}$$

where $\boldsymbol{\Omega}^* = \mathbf{e}_x$, for $\boldsymbol{\Omega} = \Omega\mathbf{e}_x$ in the present work (herein $\mathbf{e}_x$, $\mathbf{e}_y$ and $\mathbf{e}_z$ are the unit vectors in x, y, and z directions, respectively), is normalized rotation vector, $\mathbf{V} = (U, V, W)$ is dimensionless velocity vector, and $\mathbf{R} = R_y\mathbf{e}_y + R_z\mathbf{e}_z$ or

$$\mathbf{R} = [Y/E + 1 - (1+\gamma)/(4\gamma E)]\mathbf{e}_y + [Z/E - (1+\gamma)/(4E)]\mathbf{e}_z \tag{12}$$

is the dimensionless radial position vector. In equation (12), $(\mathbf{V}\cdot\nabla)\boldsymbol{\xi}$ is the vorticity convection term, $(\boldsymbol{\xi}\cdot\nabla)\mathbf{V}$ the vortex stretching, $\mathbf{V}^2\boldsymbol{\xi}$ the diffusion term, and $2J(\mathbf{e}_x\cdot\nabla)\mathbf{V}$ and $Gr_\Omega\nabla\times(\mathbf{R}\theta)$ are the vorticity generation by the Coriolis and centrifugal-buoyancy effects, respectively. Expanding these two terms, one has

$$2J(\mathbf{e}_x\cdot\nabla)\mathbf{V} = -2J[(\partial U/\partial X)\mathbf{e}_x + (\partial V/\partial X)\mathbf{e}_y + (\partial W/\partial X)\mathbf{e}_z] \tag{13a}$$

and

$$-Gr_\Omega\nabla\times(\mathbf{R}\theta) = Gr_\Omega[(R_y\,\partial\theta/\partial Z - R_z\partial\theta/\partial Y)\mathbf{e}_x + (R_z\,\partial\theta/\partial X)\mathbf{e}_y - (R_y\,\partial\theta/\partial X)\mathbf{e}_z]. \tag{13b}$$

The above equations can illuminate some aspects of rotational and thermal effects on the spatial variations of the flow fields. From equation (13a), it is evident that the velocity gradients are the sources of Coriolis generation. The longitudinal component denoted by $2J\,\partial U/\partial X$ is strong in the inlet region due to entrance effect. As the fluid flows downstream, however, the velocity gradients are alleviated during the developing procedure. For hydrodynamically fully-developed flow, the axial flow gradient becomes zero, i.e. $\partial U/\partial X = \partial V/\partial X = \partial W/\partial X = 0$, the Coriolis contribution in vorticity generation disappears. Similar point has also been mentioned by Morris [25].

Mechanisms of the centrifugal-buoyancy effect in the developing and developed flows are proposed in the following text. It is observed that the vorticity generation by the centrifugal buoyancy is closely related to the temperature gradients. For an isothermal ($\theta \equiv$ constant) flow field, the centrifugal force can only modify the pressure field but has no contribution to the vorticity generation. For non-isothermal flow in a duct of *UWT*, the temperature field has steep gradients near the inlet, but the fluid temperature is expected to increase and approach the wall temperature gradually as the flow becomes thermally fully developed. In the course of the development, referring to the axial vorticity generation $(R_y\,\partial\theta/\partial Z - R_z\,\partial\theta/\partial Y)$ in equation (13b), the vorticity generation by the centrifugal buoyancy gradually diminishes for the attenuation of both temperature gradients $\partial\theta/\partial Y$ and $\partial\theta/\partial Z$. For ducts of iso-flux walls, even the thermally fully-developed condition is reached, the fluid temperature gradients are still significant. Therefore, in an iso-flux duct, the vorticity generation by centrifugal buoyancy always exists in fully-developed flow. Furthermore, since the axial gradient of flow temperature, $\partial\theta/\partial X$, becomes zero at the thermally fully-developed condition for either UWT or UHF walls, the Y- and Z-components of vorticity generation in equation (13b) both vanish.

3. Numerical procedures

The present problem is solved numerically by a vorticity–velocity method for three-dimensional parabolic

flow [26, 27]. For a given combination of parameters, J, Gr_Ω, γ, E and Pr, the field solutions are calculated by a marching technique based on the DuFort–Frankel scheme [28]. Details of the solution procedure have been described elsewhere [4], and are not repeated here. At each axial location, iteration is performed until the specified stopping criterion, $\varepsilon = \mathrm{Max}|\phi^{m+1} - \phi^m|/\mathrm{Max}|\phi^{m+1}| < 10^{-5}$, is reached, where ϕ stands for each one of the dependent variables and m for iteration number.

To examine the grid dependence of the numerical results, a numerical experiment was performed with various grid distributions in cross-section plane ($M \times N$) and axial step size (ΔX^*). In this work, the grid lines were uniformly arranged in the cross plane, since the secondary vortices may migrate in the plane and the vortex centers change at each cross plane along the axial direction. The steep velocity gradients may appear in the fluid rather than the near-wall region only. In the axial direction, the grid is nonuniformly distributed for the uneven variations of field properties in the entrance region. Table 1 presents the results of the local Nusselt number Nu and friction factor fRe for three grid systems. It is found from Table 1 that the deviations in Nu and fRe calculated with $\Delta X^* = 1 \times 10^{-5} \sim 5 \times 10^{-4}$ M (Y-dir.) $\times N$ (Z-dir.) $= 41 \times 41$ and 51×51 are always less than 3%. Furthermore, the deviations in local Nu and fRe calculated on the grids of 41×41 with $\Delta X^* = (2 \times 10^{-6} \sim 5 \times 10^{-4})$ and $(1 \times 10^{-5} \sim 5 \times 10^{-4})$ are all less than 1%. Accordingly, the grid of $M \times N$ $(\Delta X^*) = 41 \times 41$ $(1 \times 10^{-5} \sim 5 \times 10^{-4})$ can be regarded as sufficient for the present simultaneously developing mixed convection.

As a partial verification of the computational procedure described above, the hydrodynamically developing forced convection in rectangular ducts was computed. The results are compared with the previous one [23], and it is found that the apparent friction factors agree to within 2% at all axial locations. In addition, the validity of the present solution procedure had been demonstrated in a previous study for radially rotating ducts [4].

4. Results and discussion

4.1. Comparison with previous results of rotating parallel ducts

In Fig. 2, the present predictions of peripheral average of Nu in an iso-flux duct of $\gamma = 0.5$ are plotted and compared with the computations and measurement by Levy et al. [22] and Neti et al. [21]. The computations of Levy's group considered the axial variation of the parameters, i.e. $1490 < Re < 2370$ and $0.07 < Ro < 0.26$, of which the values of Re and Ro decrease from the inlet. Therefore, the value of rotational Reynolds number at the inlet is calculated as $J = Re\,Ro = 2370 \times 0.26 \approx 616$. In our formulation the parameters are constants and the results of $J = 600$ are shown in Fig. 2. It is noted that the present results agree well with both the computations and measured data of Levy's group for $Gr_\Omega < 1 \times 10^6$. Beyond this value, the measured data behave anomalous, and the computation is hard to bring about convergence, either. Obviously, at this high Gr_Ω condition, the flow instabilities emerge. Generally speaking, the methodology employed gives very reasonable predictions of the present flow configuration.

4.2. Axial evolution of secondary vortices (UWT)

Figure 3(a), (b) and (c) show the axial developments of the cross-flow in an isothermally heated (UWT) square duct ($\gamma = 1$) with rotational parameters $(J, Gr_\Omega) = (600, 1 \times 10^4)$, $(800, 1 \times 10^4)$ and $(600, 2 \times 10^4)$, respectively. The axial variable is defined as $X^* = x/(PrReD_e)$. Each of the velocity vectors in the cross-flow plane is composed of the velocity components in the y- and z-directions. In the region near the inlet, the flow is of boundary-layer type, the fluid is repelled from the near-wall region toward the center of the duct for the boundary layer displacement effect, see the cross-flow at $X^* = 4 \times 10^{-4}$. The spiral pattern of the cross-flow there shows a tendency of vortex formation. At the axial locations of $X^* = 0.0251$ and 0.04, the primary vortex

Table 1
Comparison of local Nu and fRe on various grids for $J = 600$, $Gr_\Omega = 1 \times 10^4$, $\gamma = 1$ and $\Delta X^* = 1 \times 10^{-5}$–$5 \times 10^{-4}$

	X^*							$f\,Re$						
$M \times N$	0.001	0.005	0.010	0.040	0.080	0.100	0.300	0.001	0.005	0.010	0.040	0.080	0.100	0.300
31×31	14.30	6.35	4.97	4.49	4.25	3.99	3.04	41.62	23.38	20.27	18.36	16.77	16.36	14.29
41×41	12.95	6.28	4.95	4.64	4.29	4.00	3.05	39.00	23.30	20.27	18.75	16.92	16.47	14.34
51×51	12.58	6.25	4.94	4.80	4.32	3.05	3.05	38.17	23.28	20.28	19.03	17.00	16.53	14.36

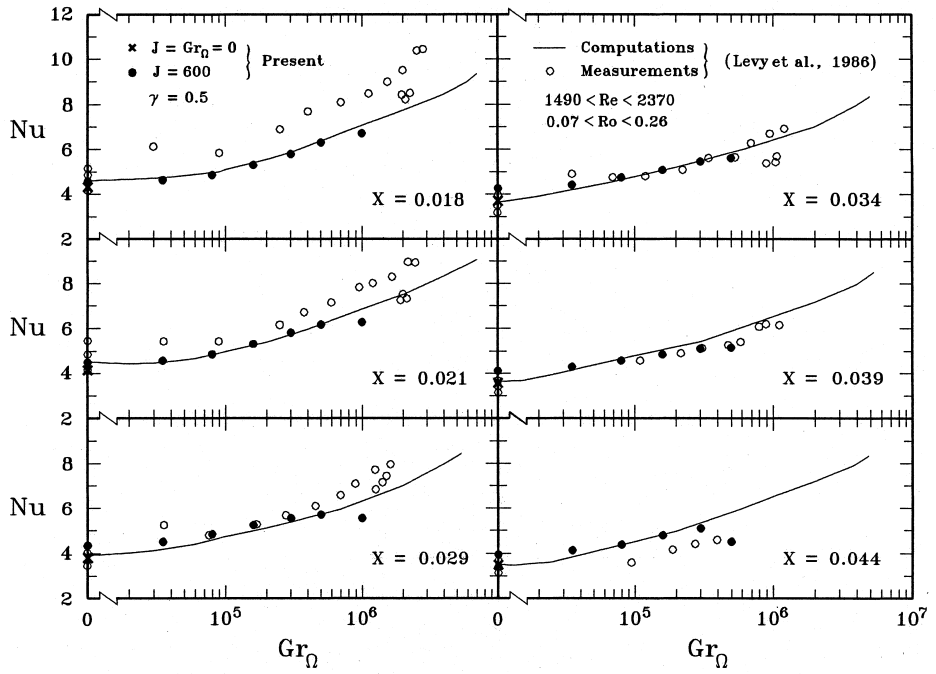

Fig. 2. Comparison of predicted and measured peripherally-averaged Nusselt numbers in an iso-flux duct of $\gamma = 0.5$ for $J = 600$ (*UHF*).

develops a severe asymmetry and the vortex core migrates. Meanwhile, the relatively weak vortices near the corners grow continuously. Further downstream, at $X^* = 0.1$, the vortices become weak. As analyzed in the previous section about equation (13), Coriolis and centrifugal buoyancy effects both diminish in the simultaneously developing flow. Therefore, secondary vortices fade away downstream and the flow field approaches the fully-developed condition.

Coriolis effect on the secondary flow can be illustrated by examining the cross-flow patterns for a rather higher rotational Reynolds number, $J = 800$, in Fig. 3(b). The comparison in Fig. 3(a) and (b) reveals that, near the entrance, e.g. $X^* \leqslant 0.01$, the flow pattern for $J = 800$ is more twisted and therefore has more potential for formation of the secondary vortices. In the subsequent axial locations, it is evident that the secondary motion for $J = 800$ is relatively stronger due to larger Coriolis effect, and the flow pattern is more complex. For example, an anomalous multi-vortex cross-flow map emerges at $X^* = 0.0251$. As in Fig. 3(a), the secondary motion also fades away in the far downstream portion of the duct. To explore the thermal effect on the vortex evolution, cross-flow map for $Gr_\Omega = 2 \times 10^4$ are plotted in Fig. 3(c) and used to compare with the solutions of $Gr_\Omega = 1 \times 10^4$ in Fig. 3(a). The stronger centrifugal buoyancy enhances the strength of the primary vortex as well as changes the position of the vortex core.

4.3. Axial velocity and temperature distributions (*UWT*)

The developing axial velocity profiles along the center line $Y = 0.5$ at various flow/thermal conditions are shown in Fig. 4(a) to (c), wherein the curves *A*, *B*, *C*, *D*, *E* and *F* denote profiles at $X^* = 4 \times 10^{-4}$, 0.01, 0.0251, 0.04, 0.1 and 2.0, respectively. An overall inspection discloses that the velocity profile near the entrance (curve *A*) is fairly uniform over the cross section. As the flow develops, the velocity in the core region is accelerated due to the entrance effect (curve *B*). Further downstream, the velocity profile is distorted due to the secondary flow effect (curves *C*, *D* and *E*). Finally, the velocity profile (curve *F*) becomes a parabolic shape, which is a typical fully-developed flow. The severe distortion of the velocity curves in developing region is due to the interaction of the centrifugal buoyancy and Coriolis effects. The corresponding temperature distributions along *Z*-direction in the plane of $Y = 0.5$ are presented in Fig. 4(d) to (f). Similar to the axial velocity distributions, the developing temperature profiles *C*, *D* and *E*, strongly depend on the parameters *J* and Gr_Ω. In general, the temperature gradients at walls are very large in inlet region and atten-

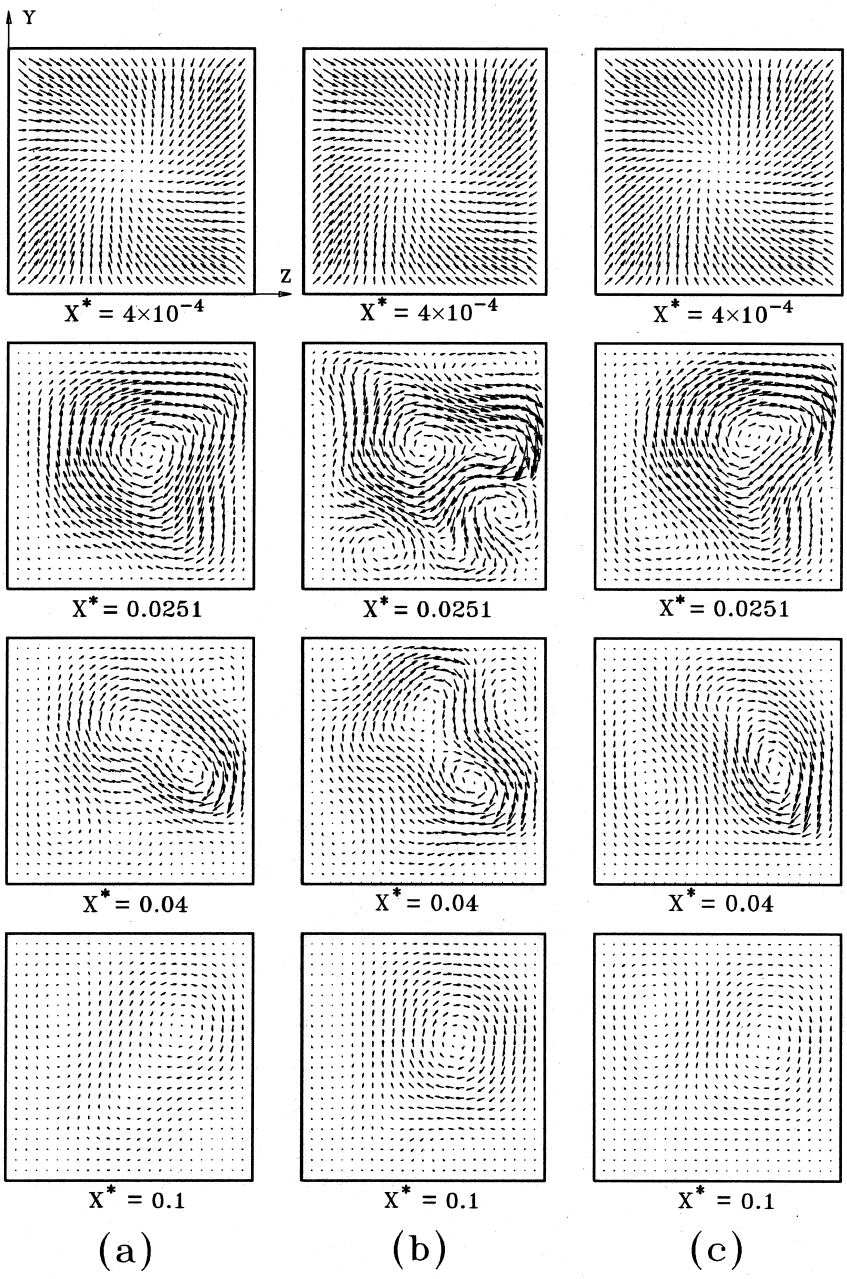

Fig. 3. Secondary flow patterns in a square duct of isothermal walls: (a) $J = 600$ and $Gr_\Omega = 1 \times 10^4$; (b) $J = 800$ and $Gr_\Omega = 1 \times 10^4$; (c) $J = 600$ and $Gr_\Omega = 2 \times 10^4$.

uated downstream due to decaying of the secondary vortices.

4.4. Axial variation of friction factors and heat transfer rates at each wall (UWT)

The parameters $(fRe)_j$ and Nu_j are employed to denote local friction factors and Nusselt numbers averaged on each wall at a fixed X^*. The values of the subscript j can be 1 and 4 for leading and trailing walls in the sense of rotation, and 2 and 3 for two side-walls as shown in Fig. 5, in which the results for the UWT case of $J = 600$, $Gr_\Omega = 1 \times 10^4$ and $\gamma = 1$ are plotted. It is observed that the values of the friction and heat transfer rates at each wall depend on the local secondary flow effect on each wall. For example, at $X^* = 0.025$ (or 0.04), the largest

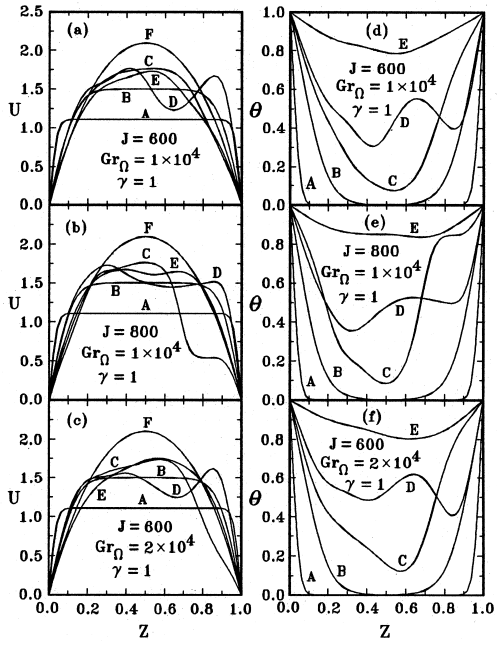

Fig. 4. Rotational effects on evolution of axial velocity and temperature fields (UWT).

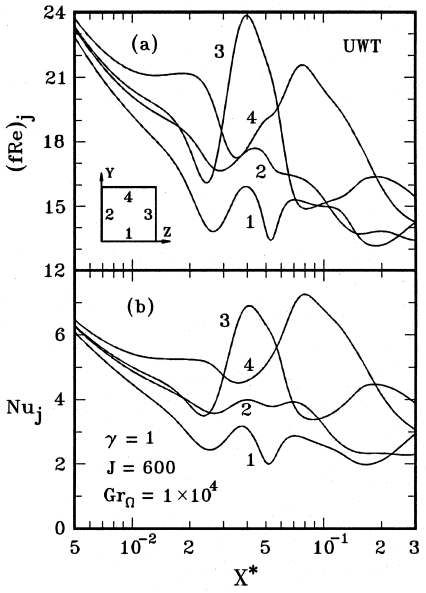

Fig. 5. Local averages of friction factors and Nusselt numbers at four walls of a square duct with $J = 600$ and $Gr_\Omega = 1 \times 10^4$ (UWT).

fRe and *Nu* emerge on wall 4 (or wall 3). It can be illuminated by examining the cross-flow patterns in Fig. 3(a), in which the secondary vortex sweeps wall 4 at $X^* = 0.0251$ and raises the friction and heat transfer on it. While at $X^* = 0.04$, the vortex core migrates to a location near wall 3 and enhances the transport rates there.

4.5. Axial variation of peripherally-averaged friction factors and heat transfer rates (*UWT*)

The Coriolis force effects on the axial distribution of the peripherally-averaged friction factor and Nusselt number are shown in Fig. 6. As a reference, the results of forced convection without rotational effects denoted by $J = Gr_\Omega = 0$ are also included in the two subplots 6(a) and 6(b). The decreases in local values of *fRe* and *Nu* near the inlet are attributed to the forced-convection entrance effect; and the deviation of the results for $J \geqslant 200$ from the forced convection one are caused by the rotational effects. It is clear that the effects of entrance and rotation are balanced out and a local minimum *fRe* (*Nu*) appears. Locations of the local minimum, which depending on the rotational effects, in *fRe* (*Nu*) curves denote the formation of the secondary vortices. Subsequently, the rotational effect dominates over the entrance effect and the *fRe* (*Nu*) increases until a local maximum value of *fRe* (*Nu*) is reached. After that, *fRe* (*Nu*) presents obvious wavy feature under strong effect of rotation, e.g. $J = 600$ and 800. This wavy behavior is related to the emergence and decay of the secondary vortices. Finally, the curves of *fRe* and *Nu* fall asymptotically to the values for forced convection when the

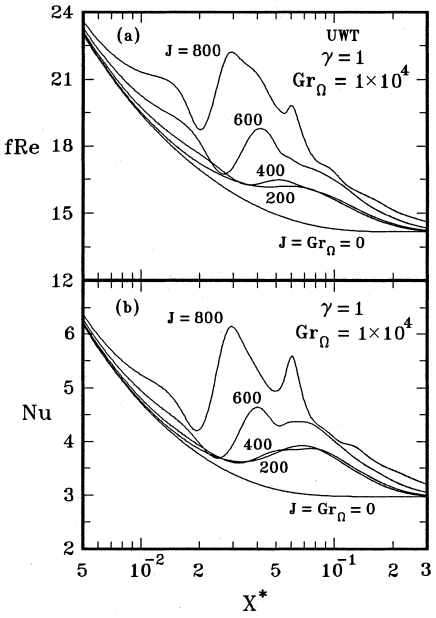

Fig. 6. Coriolis effects on the streamwise variation of peripherally-averaged friction factors and Nusselt numbers for $\gamma = 1$ and $Gr_\Omega = 1 \times 10^4$ (UWT).

velocity and temperature fields approach the fully developed condition. In addition, the larger *fRe* and *Nu* appear for a larger J due to the stronger Coriolis effect. It should be emphasized that as $J \leqslant 400$, although the centrifugal buoyancy is noticeable, the effect of J on the *fRe* and *Nu* are relatively small. This means that, for $J \leqslant 400$, the Coriolis effect in a square duct can be neglected.

Figure 7 presents the other rotational force effects, the centrifugal buoyancy, on the *fRe* and *Nu* for $J = 600$ and $\gamma = 1$. It is obvious that the effect of Gr_Ω is practically negligible for $Gr_\Omega \leqslant 10^3$. The buoyancy effect contributes to the vorticity generation and therefore enhances the secondary flow effects. Figure 7 demonstrates the enhancement in *fRe* and *Nu* caused by a rotation-induced buoyancy effect.

The effects of the duct aspect ratio on the friction factor and Nusselt number are also of interest. Figure 8 shows the axial variation of *fRe* and *Nu* with rotational Reynolds number J as a parameter in the ducts of $\gamma = 0.2$, 0.5, 2 and 5. Comparing the results in Figs 6 and 8 indicates that the effects of rotational Reynolds number on the *fRe* and *Nu* are more pronounced for a square duct ($\gamma = 1$). This is owing to the relatively stronger secondary motion presented for aspect ratio $\gamma = 1$, which in turn causes a larger augmentation in *fRe* and *Nu*. Additionally, the differences in *fRe* and *Nu* between $\gamma = 5$ and $\gamma = 0.2$ are relatively small due to a relatively weak rotational effect.

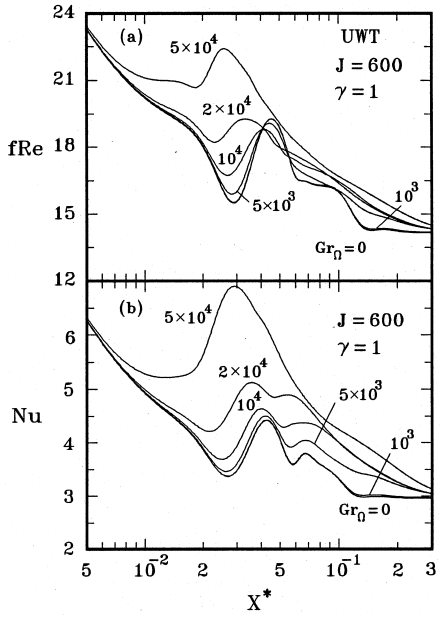

Fig. 7. Centrifugal buoyancy effects on the streamwise variation of peripherally-averaged *fRe* and *Nu* for $\gamma = 1$ and $J = 600$ (UWT).

4.6. Comparison of the UHF and UWT solutions

In Fig. 9, both UWT and UHF solutions of longitudinal vortex evolution for flow in a square duct are displayed. For the parameters of $J = 600$ and $Gr_\Omega = 1 \times 10^5$, the UWT solutions in Fig. 9(a) show the stronger secondary vortices near the inlet, i.e. $X^* = 0.01$. The vortices are dissipated along axial direction, and at a farther downstream location of $X^* = 1.0008$, the flow field is nearly fully developed and, according to the present theoretical analysis on the vorticity generation, the vortices diminish for viscous dissipation and vanishingly small vorticity generation in fully-developed region. In a UHF case, although the secondary motion in the inlet region seems weaker, the vorticity can be generated in fully-developed flow and the secondary vortices still remain even at $X^* = 1.0008$.

The difference in vortex evolution for UHF and UWT can be illustrated by examining the vorticity and the corresponding temperature contours for $J = 600$ and $Gr_\Omega = 1 \times 10^4$ in Figs 10 and 11. In the UHF case in Fig. 10, the temperature gradient, either $\partial\theta/\partial Z$ or $\partial\theta/\partial Y$, is a constant in the developing course. According to equation (13b), vorticity generation may not die out at the position of non-vanishing $\partial\theta/\partial Z$ and $\partial\theta/\partial Y$. At $X^* = 1.0008$, the axial vorticity in the Y–Z plane lies in the range $-970.93 < \xi < 970.89$. At the UWT condition, however, both $\partial\theta/\partial Z$ and $\partial\theta/\partial Y$ decrease gradually and $R_y\partial\theta/\partial Z - R_z\partial\theta/\partial Y$ does also. At $X^* = 1.0008$ (fully-developed), the axial vorticity in Fig. 11(d) is very small, i.e. $-0.4349 < \xi < 0.4317$, and the secondary motion is insignificant here. From Figs 9–11, it is observed that the developing secondary flow pattern in a rotating duct of parallel mode is asymmetric. As the flow approaches fully-developed condition, however, the flow and temperature fields tend to be symmetric with respect to the line of $Z = 0.5$, and the vorticity contours appear in an anti-symmetric pattern. Considering the asymmetric nature of the developing flow, the half domain (Y–Z plane) computations like those shown in the work of Levy et al. [21] are not appropriate for description of the local flow fields.

The effects of the secondary vortex evolution are also reflected on the axial variation of *fRe* and *Nu* in Fig. 12. As compared to the counterpart *UWT* cases in Fig. 5, more pronounced wavy variation can be observed in *fRe* and *Nu* plots. In contrast to the diminishing rotational effects at the downstream portion in Fig. 5, neither of the curves of *fRe* and *Nu* in Fig. 12 coincide with the results of a stationary duct. In Fig. 13, the results reveal that the centrifugal buoyancy effects are small in the entrance region, but become noticeable in the downstream portion. This is totally different from that of UWT cases in Fig. 6, where the buoyancy effects first grow in the entrance region and then decay as $X^* > 0.04$. The difference in the centrifugal buoyancy effects for UWT and

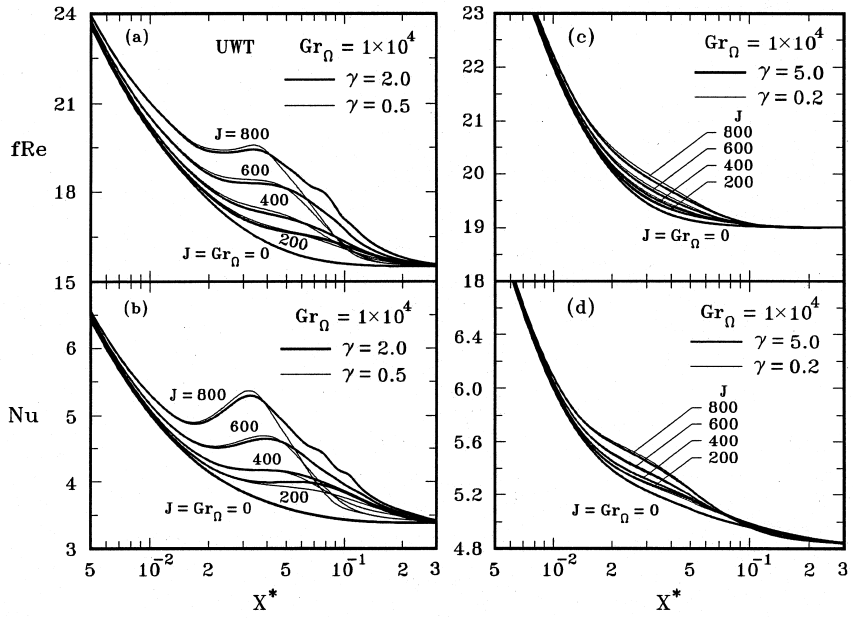

Fig. 8. Coriolis effects on the streamwise variation of peripherally-averaged friction factors and Nusselt numbers for $Gr_\Omega = 1\times10^4$ in rectangular ducts (UWT).

UHF is attributed to the distinct longitudinal evolution of the temperature field under these two kinds of thermal boundary conditions.

The above-mentioned behaviors also present in the axial evolution of $(fRe)_j$ and Nu_j for the four walls of the UHF duct. Comparison of Figs 14 and 5 shows that the differences between the transport rates of four walls tend to reduce for the diminishing temperature gradients as well as the secondary vortices in the UWT case; whereas for the UHF case in Fig. 14, the increasing temperature gradient in the downstream part results in remarkable differences in transport rates on the four walls. The largest deviation between the leading (wall 1) and the trailing (wall 4) walls reflects the presence of a vortex pair with stagnation point on the trailing wall.

5. Concluding remarks

In the present work, mixed convection flow and heat transfer in rectangular ducts rotating about a parallel axis have been explored. The development of secondary vortices and the effects of thermal boundary conditions on the flow and heat transfer have been investigated in detail by examining the local flow structure and temperature field. The following conclusions can be drawn:

(1) Formation of the secondary flow depends strongly upon the duct rotation. Vorticity can be generated by the Coriolis as well as centrifugal-buoyancy effects. The former is closely related to the axial velocity gradients and the latter to the temperature gradients. For the cases of UWT, high temperature gradients appear in the upstream region of the duct; while the temperature gradients alleviated gradually in the simultaneous development procedure. Therefore, the secondary vortices emerge first and fade away downstream. In the ducts of iso-flux (UHF) walls, secondary vortices in the entrance region are weaker than those for UWT, but the buoyancy-induced vorticity generation becomes significant in the downstream part of the duct. Both the vorticity transport analysis and the numerical results indicate that the rotational effects in iso-flux ducts are more significant than that in isothermal ones in the fully-developed flow region. The longitudinal variations of the friction factor and heat transfer performance display a similar trend as the evolution of the secondary flow. Wavy variations in local fRe and Nu arising from evolution of the secondary vortices may emerge in the cases of high rotational Reynolds numbers.

(2) Both effects of Coriolis force and centrifugal buoyancy raise the peripherally-averaged friction factors and heat transfer rates in the entrance region. The extent of augmentation in fRe and Nu increases with J and Gr_Ω. In the parameter range considered, the entrance length lies between $X^* = X/D_e PrRe = 0.3$ to 0.5. In the case of $Pr = 0.7$ and $Re = 500$, the entrance length is $L_e/D_e = 105$ to 175. Therefore, the entrance effect dominates the flow and heat transfer characteristics for a duct of $L_e/D_e \sim O(10^2)$.

(3) For the cross-sectional aspect ratio of the ducts

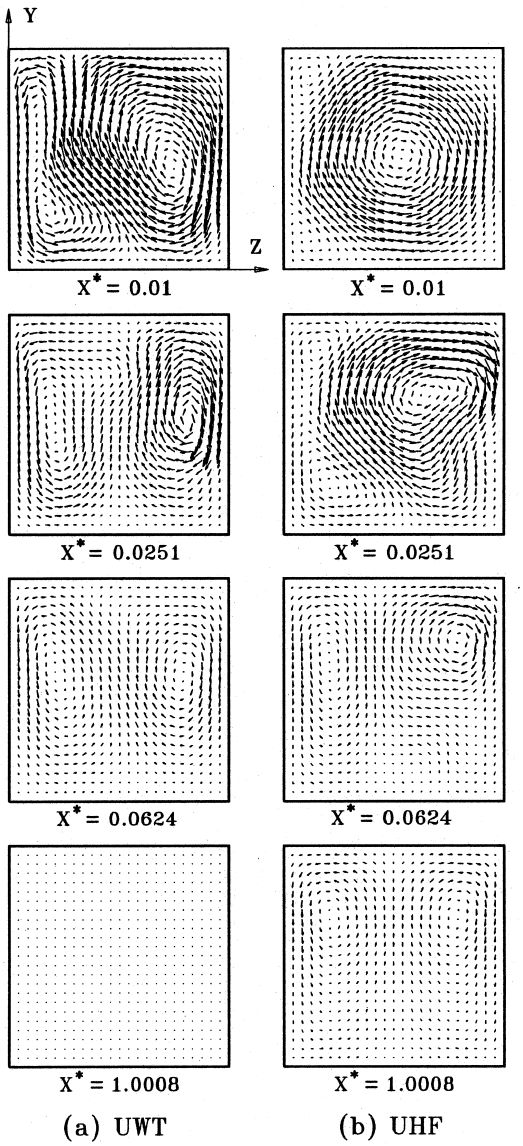

Fig. 9. Comparison of secondary flow patterns for $\gamma = 1, J = 600$ and $Gr_{\Omega} = 1 \times 10^5$. (a) UWT, (b) UHF.

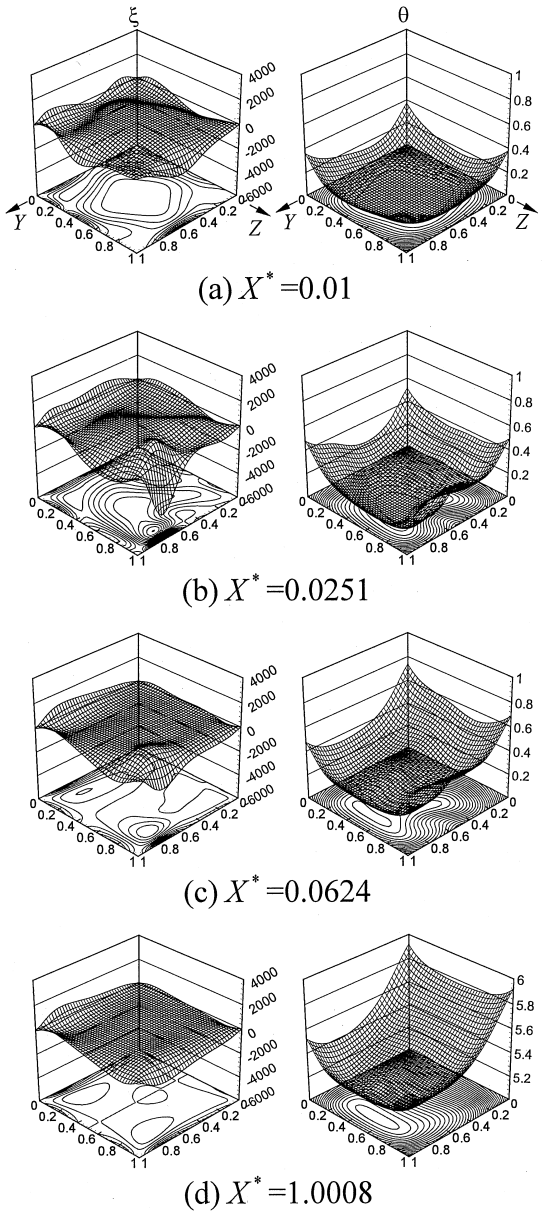

Fig. 10. Axial vorticity and temperature contours for $\gamma = 1$, $J = 600$ and $Gr_{\Omega} = 1 \times 10^4$ (UHF).

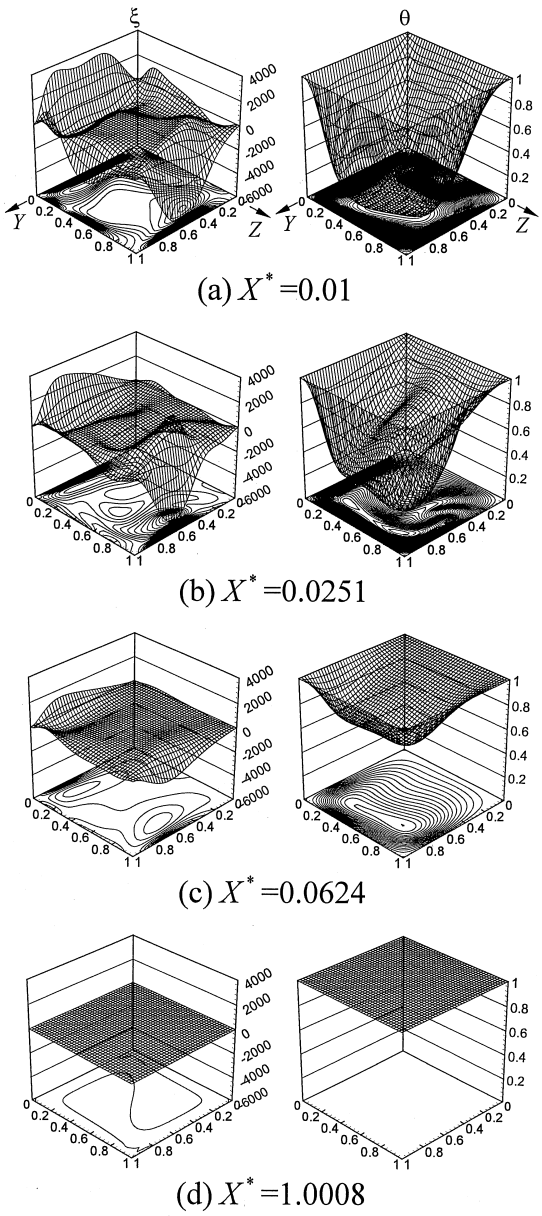

Fig. 11. Axial vorticity and temperature contours for $\gamma = 1$, $J = 600$ and $Gr_\Omega = 1 \times 10^4$ (UWT).

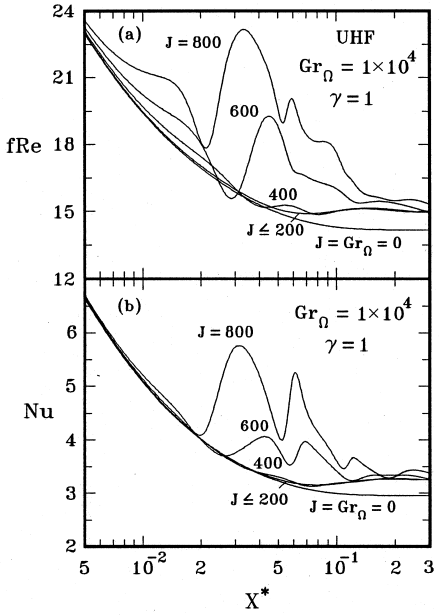

Fig. 12. Coriolis effects on the streamwise variation of peripherally-averaged *fRe* and *Nu* for $Gr_\Omega = 1 \times 10^4$ in an iso-flux square duct (UHF).

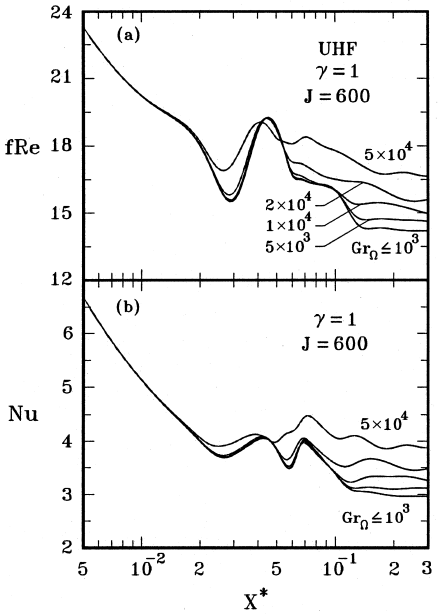

Fig. 13. Centrifugal-buoyancy effects on the streamwise variation of peripherally-averaged *fRe* and *Nu* for $J = 600$ and an iso-flux square duct (UHF).

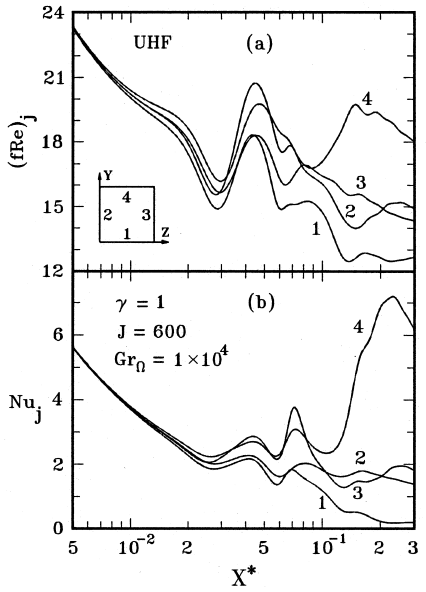

Fig. 14. Local averages of friction factors and Nusselt numbers at four walls of a square duct with $J = 600$ and $Gr_\Omega = 1 \times 10^4$ (UHF).

considered in the present study, $0.2 \leqslant \gamma \leqslant 5$, the largest rotational effects on the fRe and Nu is found in the duct of $\gamma = 1$, wherein the strongest secondary flow can be induced by rotational forces.

References

[1] S. Fann, W.J. Yang, Hydrodynamically-thermally developing laminar flow through rotating channels having isothermal walls, Num. Heat Transfer 22 (3) (1992) 257–288.

[2] T.C. Jen, A.S. Lavine, G.J. Hwang, Simultaneously developing laminar convection in rotating isothermal square channels, Int. J. Heat Mass Transfer 35 (1) (1992) 239–254.

[3] C.Y. Soong, G.J. Hwang, Laminar mixed convection in a radially rotating semiporous channel, Int. J. Heat Mass Transfer 33 (9) (1990) 604–611.

[4] W.M. Yan, C.Y. Soong, Simultaneously developing mixed convection in radially rotating rectangular ducts, Int. J. Heat Mass Transfer 38 (4) (1995) 665–677.

[5] C.Y. Soong, W.M. Yan, Numerical study of mixed convection heat transfer between two co-rotating symmetrically-heated disks, AIAA J. Thermophys. Heat Transfer 7 (1) (1993) 165–170.

[6] C.Y. Soong, W.M. Yan, Transport phenomena in non-isothermal flow between co-rotating asymmetrically-heated disks, Int. J. Heat Mass Transfer 37 (15) (1994) 2221–2230.

[7] W.D. Morris, laminar convection in a heated vertical tube rotating about a parallel axis, J. Fluid Mech. 21 (3) (1965) 453–464.

[8] Y. Mori, W. Nakayama, Forced convective heat transfer in a straight pipe rotating around a parallel axis (first report, laminar region), Int. J. Heat Mass Transfer 10 (1967) 1179–1194.

[9] W. Nakayama, Forced convective heat transfer in a straight pipe rotating around a parallel axis (second report, turbulent region), Int. J. Heat Mass Transfer 11 (1968) 1185–1201.

[10] J.L. Woods, Heat transfer and flow resistance in a rotating duct system, Ph.D. dissertation, University of Sussex, Falmer, U.K., 1975.

[11] A.R. Johnson, W.D. Morris, Pressure loss measurements in circular ducts which rotate about a parallel axis, in: Proceedings of Fourteenth ICHMT Symposium in Rotating Machinery, Dubrovnick, Yugoslavia, Hemisphere Pub., Washington, 1982, pp. 51–62.

[12] J.F. Humphrey, W.D. Morris, H. Barrow, Convection Heat transfer in the entry region of a tube which revolves about an axis parallel to itself, Int. J. Heat Mass Transfer 10 (1967) 333–347.

[13] W.D. Morris, F.M. Dias, Turbulent heat transfer in a revolving square-sectioned tube, J. Mech. Engrg Sci. 22 (1980) 95–101.

[14] A.R. Johnson, W.D. Morris, An experimental investigation into the effects of rotation on the isothermal flow resistance in circular tubes rotating about a parallel axis, Int. J. Heat Mass Transfer 13 (1992) 132–140.

[15] M. Mahadevappa, K.V.C. Rao, V.M.K. Sastri, Experimental investigation for fluid flow and heat transfer in an elliptical duct rotating about a parallel axis, Experimental Heat Transfer 6 (1993) 97–109.

[16] D. Skiadaressis, D.B. Spalding, Laminar heat transfer in a pipe rotating around a parallel axis, Report HRS/76123, Mechanical Engineering Department, Imperial College of Science and Technology, London, 1976.

[17] M. Mahadevappa, K.V.C. Rao, V.M.K. Sastri, Numerical study of laminar fully developed fluid flow and heat transfer in rectangular and elliptical ducts rotating about a parallel axis, Int. J. Heat Mass Transfer 39 (1996) 867–875.

[18] A.R. Johnson, Flow resistance in circular tubes rotating about a parallel axis, Ph.D. dissertation, University of Hull, U.K., 1988.

[19] S. Imao, Q. Zhang, Y. Yamada, The laminar flow in the developing region of a rotating pipe, JSME Int. J., Series II 32 (1989) 317–323.

[20] D.T. Gethin, A.R. Johnson, Numerical analysis of the developing fluid flow in a circular duct rotating steadily about a parallel axis, Int. J. Numer. Method in Fluids 9 (1989) 151–165.

[21] E. Neti, A.S. Warnork, E.K. Levy, K.S. Kannan, Computation of laminar heat transfer in rotating rectangular ducts, ASME J. Heat Transfer 107 (1985) 575–582.

[22] S. Levy, S. Neti, G. Brown, F. Bayat, Laminar heat transfer and pressure drop in a rectangular duct rotating about a parallel axis, ASME J. Heat Transfer 108 (1986) 350–356.

[23] R.A. Shah, A.L. London, Laminar Flow Forced Convection in Ducts, Suppl. to Adv. Heat Transfer, Academic Press, New York, 1978, pp. 196–222.

[24] S.V. Patankar, D.B. Spalding, A calculation procedure for

heat, mass and momentum transfer in three-dimensional parabolic flows, Int. J. Heat Mass Transfer 15 (1972) 1787–1806.
[25] W.D. Morris, Heat Transfer and Fluid Flow in Rotating Coolant Channels, Research Studies Pr./John Wiley and Sons, Chichester, U.K., 1981.
[26] K. Ramakrishna, S.G. Rubin, P.K. Khosla, Laminar natural convection along vertical square ducts, Num. Heat Transfer 5 (1982) 59–79.
[27] W.M. Yan, Developing flow and heat transfer in radially rotating rectangular ducts with wall-transpiration effects, Int. J. Heat Mass Transfer 37 (1994) 1465–1473.
[28] P.J. Roache, Computational Fluid Dynamics, Reinhold, New York, 1971, pp. 61–64.